Multifield-induced antiferromagnet transformation into altermagnet and realized anomalous valley Hall effect in monolayer $VPSe_3$

Hanbo Sun,[1] Pengqiang Dong,[1] Chao Wu,[1] and Ping Li[1,2,3,*]

[1]*State Key Laboratory for Mechanical Behavior of Materials, School of Materials Science and Engineering, Xi'an Jiaotong University, Xi'an, Shaanxi 710049, People's Republic of China*

[2]*State Key Laboratory of Silicon and Advanced Semiconductor Materials, Zhejiang University, Hangzhou 310027, People's Republic of China*

[3]*State Key Laboratory for Surface Physics and Department of Physics, Fudan University, Shanghai 200433, People's Republic of China*

(Received 17 March 2025; revised 2 May 2025; accepted 30 May 2025; published 13 June 2025)

Altermagnetism, as a new category of collinear magnetism distinct from traditional ferromagnetism and antiferromagnetism, exhibits the spin splitting without net magnetization. Currently, researchers are focused on searching three-dimensional altermagnetism and exploring its novel physical properties. However, there is a lack of understanding of the physical origin and valley splitting of two-dimensional altermagnetic emergent behavior. Here, we propose an approach to realize the transition from Néel antiferromagnetism to altermagnetism in a two-dimensional system using an electric field, Janus structure, and ferroelectric substrate. In monolayer $VPSe_3$, we demonstrate that multiple physical fields cause the upper and lower Se atoms unequally to break *PT* symmetry, resulting in altermagnetic spin splitting. We note that monolayer $VPSe_3$ produces a spontaneous valley splitting of 2.91 meV at the conduction band minimum. The electric field can tune the valley splitting magnitude, while the Janus structure not only changes the valley splitting magnitude, but also alters the direction. More interestingly, when the ferroelectric polarization of Al_2S_3 is P↑, the direction of valley polarization is switched and the magnitude is almost unchanged. However, the valley splitting significantly increases under the P↓. It is worth noting that the ferroelectric polarization can switch altermagnetic effect and realize anomalous valley Hall effect. Besides, we reveal the microscopic mechanism of valley splitting by an effective Hamiltonian. Our findings not only provide a method to designing the altermagnet, but also enrich the valley physics.

DOI: 10.1103/shvd-vmvs

I. INTRODUCTION

Recently, a new type of magnetism named "altermagnetism" has been proposed in condensed matter physics [1–5]. The altermagnetism has two fascinating properties, which mainly manifested as a zero net magnetic moment and spin splitting along specific high symmetry paths without the spin-orbit coupling (SOC). The discovery has not only promoted the development of spintronics, but also enriched the application scenarios of magnetic materials. For example, giant and tunneling magnetoresistance effect is raised in altermagnets [6]. Besides, the anomalous Hall effect is reported in the altermagnet RuO_2, in which the magnitude can be compared to that of the ferromagnet (FM) [7]. In addition, a new type of torque, spin splitter torque, has been theoretically proposed [8] and experimentally observed [9,10] in the altermagnet. Moreover, the heterojunctions of the altermagnet are reported to possess chiral Majorana fermion or Majorana zero energy modes [11,12]. However, these investigations have mainly focused on bulk materials [2–10,13–16], while two-dimensional (2D) altermagnets pay limited attention. How to tune the 2D antiferromagnet (AFM) into the altermagnet is even less involved [17–21], but it is crucial to understanding the origin of the emergent behavior.

In spintronics, a new degree of freedom, valley, has been proposed as the third degree of freedom beyond the electron's charge and spin [22–25]. The valley indicates a local energy minimum or maximum point in the conduction or valence band. At present, the investigation focus of valleytronics is how to realize spontaneous valley polarization and effectively tune [26–37]. There are two main ways to achieve spontaneous valley polarization, which is named ferrovalley material [26]. One approach is to break the time-reversal symmetry (*T*) with the FM or AFM [26–30,34–37], while the other way is to break the inversion symmetry (*P*) by ferroelectricity [32,33,38]. It is well known that altermagnets break the combined symmetry of the *P* and *T* (named the *PT* symmetry). Can the altermagnetism realize spontaneous valley polarization and how it differs from the FM and AFM systems?

In this article, we propose a scheme for achieving altermagnetism in a 2D system. Here, we focus on the transformation of AFM into the altermagnet by the multifield induction, such as an electric field, Janus structure, and ferroelectric substrate. It is well known that the AFM hold the *PT* symmetry. The multiple physical fields can induce the *PT* symmetry breaking, which causes the band degeneracies of spin up and spin down bands to disappear on a special high symmetrical path,

*Contact author: pli@xjtu.edu.cn

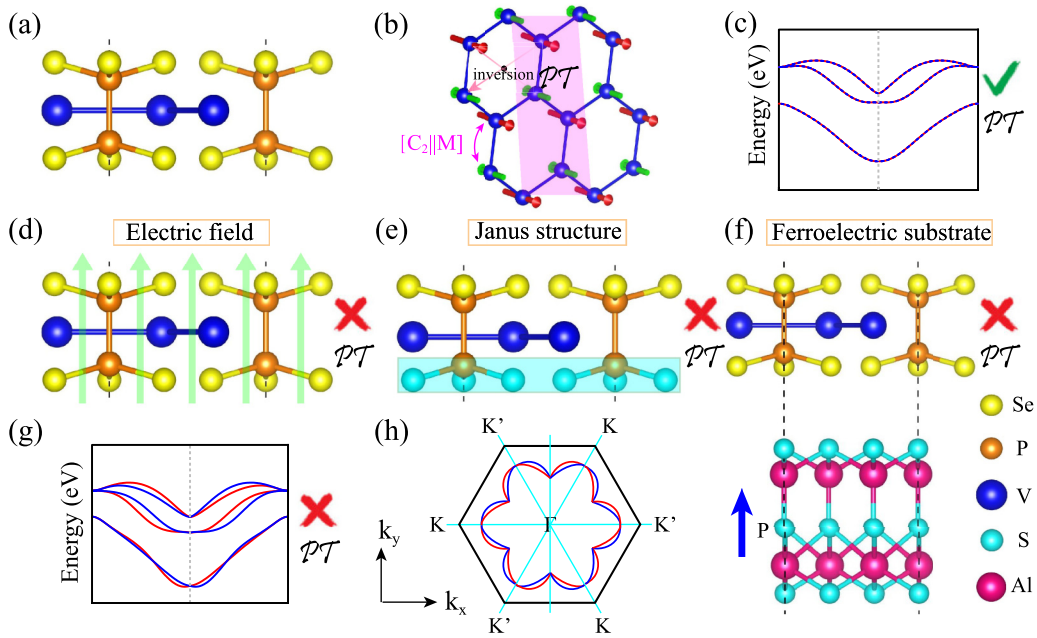

FIG. 1. (a) Side view of the crystal structure for monolayer $VPSe_3$. (b) Schematic diagram of Néel type magnetic order for monolayer $VPSe_3$ with the *PT* symmetry. (c) Band structure of AFM-N state with the *PT* symmetry. Three kinds of field induced *PT* symmetry breaking. (d) Applied an external electric field. (e) Functionalizing the crystal structure into Janus configuration form by substituting the bottom Se layer through S atoms. (f) Ferroelectric substrate is introduced to form vdW heterostructure. (g) Band structure of AFM-N state with broken *PT* symmetry. (h) The band structures show i-wave symmetry without the SOC effect. The magenta, the light blue, blue, orange, and yellow balls represent Al, S, V, P, and Se elements, respectively.

exhibiting altermagnetic characteristics. Based on the density functional theory (DFT) calculations, we demonstrate this mechanism and phenomena in monolayer $VPSe_3$. Moreover, monolayer $VPSe_3$ exhibits spontaneous valley polarization due to the combined effects of SOC and *T* symmetry breaking. The electric field can tune the magnitude of valley splitting, while the Janus structure (built-in electric field) and ferroelectric substrate can regulate not only the magnitude but also the direction and position of valley polarization. In addition, the ferroelectric polarization can switch altermagnetic effect and realize anomalous valley Hall effect. Our work provides another direction for investigating altermagnetism and valleytronic devices.

II. RESULTS AND DISCUSSION

A. Structure and symmetry

As shown in Fig. 1(a), it shows the crystal structure of monolayer $VPSe_3$, which is six Se atoms nearest to each V atom. The monolayer $VPSe_3$ shows a hexagonal honeycomb lattice with the point group of D_{3d} and space group of $P\bar{3}1m$. The optimized lattice constant of $VPSe_3$ is 6.24 Å. When magnetic order is not considered, monolayer $VPSe_3$ has the *P* symmetry. However, since the magnetic ground state of $VPSe_3$ is Néel AFM, both the *P* and *T* symmetry are broken. Despite this, invariance is exhibited when the spatial inversion and time reversal occur simultaneously, that is, the *PT* symmetry [see Fig. 1(b)]. It is well established that a system with *PT* symmetry exhibits Kramers degeneracy in its band structure. Namely, as shown in Fig. 1(c), the spin up and spin down bands are degenerate. Besides, the opposite spin sublattices are jointed by the combined rotation and mirror symmetry, denoted as $[C_2\|M]$. The $[C_2\|M]$ symmetry leads to $E(s,\mathbf{k}) = [C_2\|M]E(s,\mathbf{k}) = E(-s, M\mathbf{k})$, which plays a vital role in realizing altermagnetism. Here, the *s*, $\mathbf{k}$, and $E(s,\mathbf{k})$ represent the spin, momentum, and spin- and momentum-dependent bands, respectively.

Here, we propose three kinds of fields to break the *PT* symmetry. As shown in Figs. 1(d)–1(f), these include the application of out-of-plane external electric fields, the functionalizing crystal structure into Janus configuration form by substituting the bottom Se layer through S atoms, and the applied ferroelectric substrate. A common feature of these three methods is that the mirror symmetry can be preserved. Consequently, as shown in Fig. 1(g), the Kramers degeneracy is lifted and the band structure characteristics of altermagnet are exhibited. More interestingly, as shown in Fig. 1(h), the i-wave altermagnets are formed.

B. Band structure and valley splitting

To determine the magnetic ground state of monolayer $VPSe_3$, as shown in Fig. S1 [39], we consider four possible magnetic configurations in the $2 \times 2 \times 1$ supercell, ferromagnetic (FM), antiferromagnetic Néel (AFM-Néel), antiferromagnetic stripy (AFM-stripy), and antiferromagnetic zigzag (AFM-zigzag). We calculate that the FM, AFM-stripy, and AFM-zigzag states have 1110.69 meV, 341.39 meV, and 656.59 meV more energy than the AFM-Néel state, respectively, which indicates that the AFM-Néel phase is the magnetic ground state of monolayer $VPSe_3$ (see Table SI) [39]. For the 2D magnetic materials, the out-of-plane

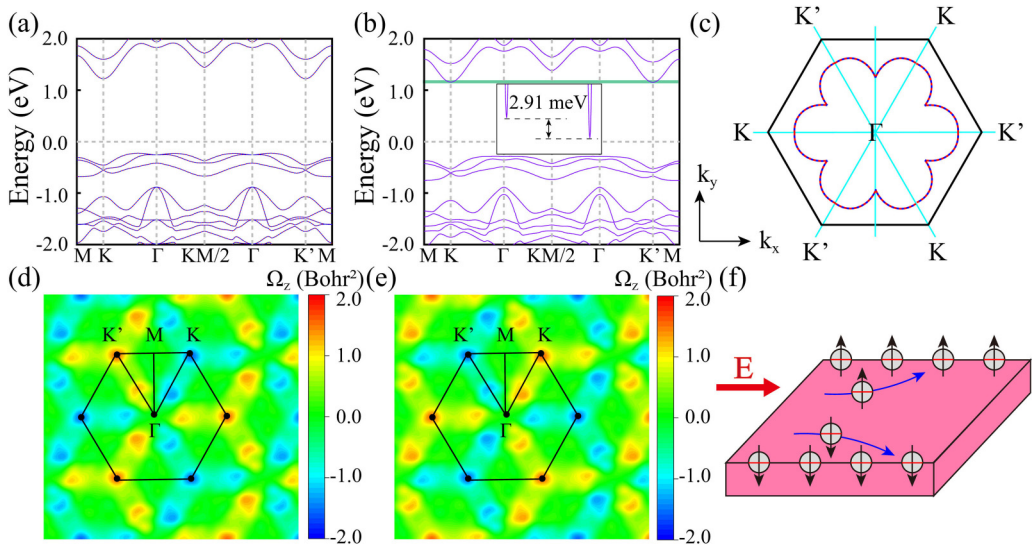

FIG. 2. (a) Spin-polarized band structure of monolayer $VPSe_3$. The solid red line and dashed blue line represent spin up and spin down bands, respectively. (b) The band structures with the SOC effect. The valley splitting of conduction band is exhibited by the green shading. (c) The valence band at around −1.2 eV. The Berry curvatures of monolayer $VPSe_3$ for (d) spin up state and (e) spin down state in the entire Brillouin zone. (f) Schematic diagram of spin-valley Hall effect in the electron-doped monolayer $VPSe_3$ at the K' valley. The electrons and holes are shown by the − and + symbol. The ↑ and ↓ represents the spin up and spin down carriers, respectively.

magnetic anisotropy energy (MAE) is the basis for their stable existence [40,41]. The MAE is defined as $\mathrm{MAE} = E_{100} - E_{001}$, where E_{100} and E_{001} represent the total energy of the magnetic moment along the [100] and [001] axes, respectively. The calculated MAE is 0.10 meV, which indicates the easy magnetization direction along the [001] axis.

Then, we calculate the spin-polarized band structure of monolayer $VPSe_3$. As shown in Fig. 2(a), the spin up and spin down bands are degenerate, in which the *PT* symmetry induces the Kramers degeneracy. It is worth noting that the K/K' valley of conduction band minimum (CBM) is degenerate. Note that Fig. 2(c) plots the valence band at around −1.2 eV. When the SOC is switched on, as shown in Fig. 2(b) and Fig. S2 [39], the energy valley degeneracy of K and K' disappears, resulting in 2.91 meV spontaneous valley splitting. Since the splitting of the valence valley is not strictly symmetrical, we will not conduct the research on this (see Fig. S2) [39]. Here, we define valley splitting as the energy difference between K and K' points. The origin of valley splitting in monolayer $VPSe_3$ is consistent with the previously reported magnetic system due to the combined T symmetry broken and SOC effect. To understand the orbital composition of valley splitting, we calculate the orbital-resolved band structure of monolayer $VPSe_3$. As shown in Fig. S3 [39], the valence band maximum (VBM) bands are mainly contributed by the $d_{x^2-y^2} + d_{xy} + d_{z^2}$ orbitals of V atoms, while the CBM bands are dominated by the $p_x + p_y$ orbitals of Se atoms.

Based on the derivation of the effective Hamiltonian model [39], the energy level of the CBM valley can be written as $E_c^\tau = \langle \psi_c^\tau | \hat{H}^0_{\mathrm{SOC}} | \psi_c^\tau \rangle$. Consequently, the valley splitting can be described as

$$E_c^K - E_c^{K'} = i\langle p_x | \hat{H}^0_{\mathrm{SOC}} | p_y \rangle - i\langle p_y | \hat{H}^0_{\mathrm{SOC}} | p_x \rangle \approx \lambda, \qquad (1)$$

where $\hat{L}_z|p_x\rangle = \mathrm{i}\hbar|p_y\rangle$ and $\hat{L}_z|p_y\rangle = -\mathrm{i}\hbar|p_x\rangle$.

In addition, we understand valleys in terms of Berry curvature. Since monolayer AFM $VPSe_3$ is protected by *PT* symmetry, the Berry curvature is zero for the entire Brillouin zone. Therefore, we calculate the Berry curvature of spin up and spin down states. As shown in Figs. 2(d) and 2(e), the Berry curvature has equal magnitude at the K and K' points, while it shows opposite signs for the same valley of different spin states and different valleys of the same spin state. When the Fermi level shifts the conduction band of the K' valley by electron doping, the spin up electrons from the K' valley will be accumulated at the right edge of the sample, while the spin down electrons from the K' valley will shift to the left edge under an in-plane electric field. As shown in Fig. 2(f), we name the phenomenon the spin-valley Hall effect.

C. Electric field induced transformation into the altermagnet

From the perspective of device applications, the electric field stands out as the most effective means for tuning the physical quantity [42,43]. This modulation method not only responds swiftly but also avoids causing damage to the materials themselves, demonstrating unique advantages in the application of micro- and nanodevices. Therefore, we investigate the effect of electric field on monolayer $VPSe_3$. Here, instead of reoptimizing $VPSe_3$ structure, we apply an electrostatic potential to monolayer $VPSe_3$. This causes the upper and lower Se atomic layer to be inequivalent, resulting in the broken *PT* symmetry. In the absence of the SOC effect, the band structure holds sixfold rotational symmetry (C_6). The $E(s, \mathbf{k}) = E(-s, -\mathbf{k})$ relationship is satisfied on special high symmetric lines. However, the rotational symmetry of band structure will be reduced to threefold (C_3) under the SOC effect.

First, we investigate the magnetic ground state at 0.0–0.3 V/Å. As shown in Fig. S4 [39], the effect of the

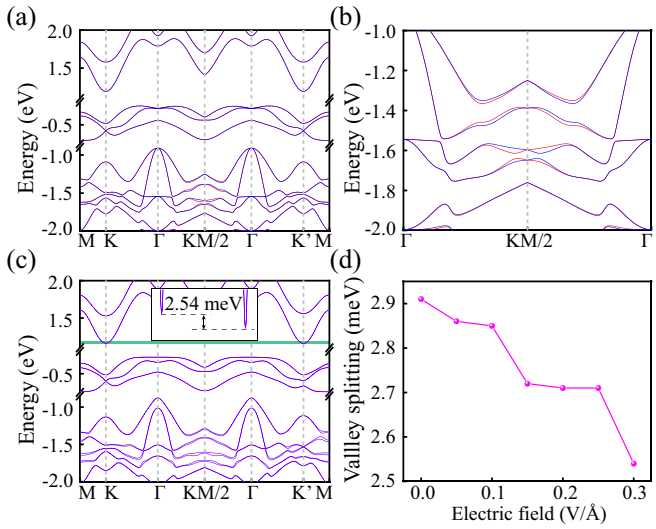

FIG. 3. (a) Spin-polarized band structure of monolayer $VPSe_3$ under an external electric field of 0.3 V/Å. The solid red and blue lines denote spin up and spin down bands, respectively. (b) An enlarged view of the region around $KM/2$ in (a). (c) The band structures with the SOC effect under an external electric field of 0.3 V/Å. The valley splitting of conduction band is shown by the green shading. (d) The valley splitting of monolayer $VPSe_3$ as a function of the external electric field.

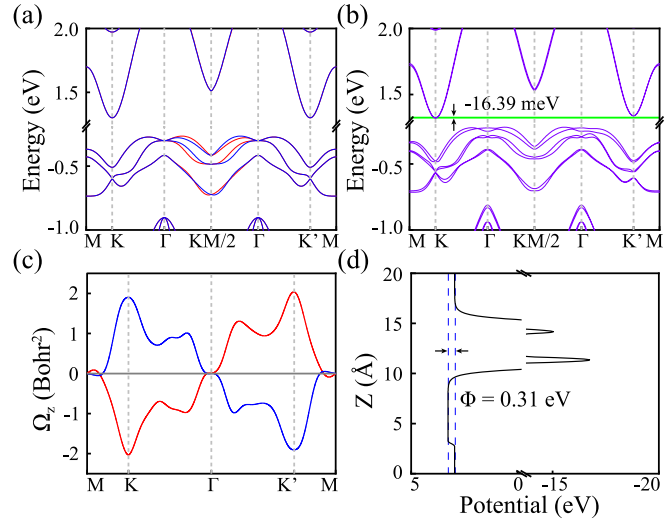

FIG. 4. (a) Spin-polarized band structure of Janus $V_2P_2S_3Se_3$. The solid red and blue lines represent spin up and spin down bands, respectively. (b) The band structures of Janus $V_2P_2Se_3S_3$ with the SOC effect. The valley splitting of conduction band is exhibited by the green shading. (c) The Berry curvature along the high symmetry line. The red and blue lines represent Berry curvatures of spin up and spin down states, respectively. (d) The planar averaged electrostatic potential of Janus $V_2P_2S_3Se_3$.

electric field on the energy difference between FM and AFM states is only 0.1 meV, which means that the AFM phase is still the magnetic ground state. To confirm the symmetry analysis, we calculate the band structure at an electric field of 0.3 V/Å. As shown in Fig. 3(a), both valence and conduction bands of the valley at K and K' points is completely degenerate, which verifies that the band structure has C_6 symmetry without the SOC effect. More interestingly, as shown in Fig. 3(b), the spin splitting is exhibited at the $\Gamma-KM/2-\Gamma$ path. It is the typical characteristic of the altermagnet, which the AFM material does not have. Moreover, when the SOC is included, the valley splitting of 2.54 meV is still observed at the CBM. Since the valley degeneracy of K and K' points disappears, the symmetry decreases from C_6 to C_3. It also demonstrates our symmetry analysis. Besides, as shown in Fig. 3(d), the change of valley splitting is only 0.4 meV at 0.0–0.3 V/Å. It is mainly because the splitting valley is contributed by the nonmagnetic Se atom.

D. Janus structure induced transformation into the altermagnet

The second approach is that it actually makes the upper and lower Se atomic layers unequal. We use the S atom to replace the lower Se atom to form the Janus structure $V_2P_2S_3Se_3$. For the Janus $V_2P_2S_3Se_3$, we also consider four possible magnetic configurations, as shown in Fig. S1 [39]. The calculation results show that the AFM-Néel state is 1343.10 meV, 428.20 meV, and 818.07 meV lower than the FM, AFM-stripy, and AFM-zigzag states, respectively. This implies that the magnetic ground state of the Janus structure $V_2P_2S_3Se_3$ remains AFM-Néel. Note that the Janus structure not only failed to weaken the AFM-Néel state, but rather enhanced it.

To enrich the physical properties of 2D materials, Zhang *et al*. has successfully prepared Janus graphene as early as 2013 [44]. After more than 10 years of development, the current technology for preparing 2D Janus structures has been very mature and successfully synthesized Janus transition metal dichalcogenides (TMDs), such as MoSSe [45], WSSe [46], Janus MXenes [47], etc. Due to the asymmetry between the lower and upper surfaces of the Janus structure, a significant built-in electric field is produced. Therefore, it naturally breaks the PT symmetry. We speculate that the same phenomenon of $VPSe_3$ applied electric field will be generated in $V_2P_2S_3Se_3$.

In the absence of SOC, as shown in Fig. 4(a), the significant spin splitting is clearly observed in the $\Gamma-KM/2-\Gamma$ path. It indicates that the AFM to altermagnet transition is realized by constructing the Janus structure without the PT symmetry. In addition, the CBM at the K and K' points exhibits valley degeneracy. When the SOC is switched on, as illustrated in Fig. 4(b), the K and K' valley degeneracies disappear, producing valley splitting up to -16.39 meV. It demonstrates that the intrinsic spontaneous valley polarization is achieved in the altermagnet monolayer $V_2P_2S_3Se_3$. Besides, to understand the valley related physics, we calculate Berry curvature of the monolayer $V_2P_2S_3Se_3$. As shown in Fig. 4(c), the Berry curvature of spin up exhibits a negative value near the K point and a positive near the K' point. On the contrary, the Berry curvature of spin down is completely reversed sign. It is also the characteristic of valley degeneracy. To further understand the valley splitting of monolayer $V_2P_2S_3Se_3$ -16.39 meV, we introduce the built-in electric field $E_{\text{in}} = (\Phi_2 - \Phi_1)/\Delta h$, where Φ_1, Φ_2, and Δh represent the electrostatic potential at the upper surface and lower surface and structural height of $V_2P_2S_3Se_3$, respectively. As shown in Fig. 4(d), the built-in

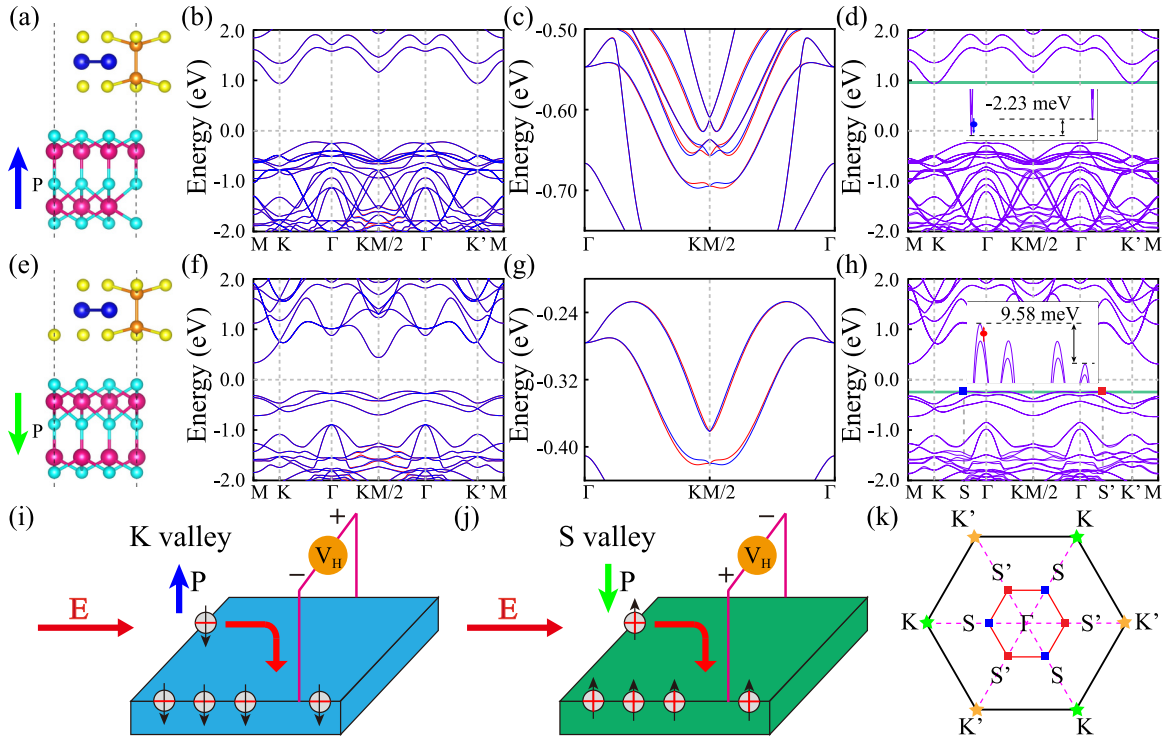

FIG. 5. (a), (e) Side views of $VPSe_3/Al_2S_3$ heterostructures with the top-S configuration. Panels (a) and (e) correspond to the upward and downward polarization of Al_2S_3, respectively. (b), (f) Spin-polarized band structure of $VPSe_3/Al_2S_3$ for (b) the P↑ state and (f) the P↓ state with the top-S configuration. The solid red and blue lines represent spin up and spin down bands, respectively. Panels (c) and (g) exhibit the enlarged view of the region around $KM/2$ for (b) and (f). (d), (h) Band structure of $VPSe_3/Al_2S_3$ heterostructures with the SOC effect for (d) the P↑ state and (h) the P↓ state with the top-S configuration. The green shading shows the valley splitting. (i), (j) Schematic diagrams of anomalous valley Hall effect in (i) the electron-doped monolayer $VPSe_3$ at the K valley and (j) the hole-doped at the S valley, respectively. The electrons and holes are represented by the $-$ and $+$ symbol. The ↑ and ↓ denote the spin up and spin down carriers, respectively. (k) Location of K/K' and S/S' valleys in the first Brillouin zone.

electric field is 0.10 V/Å by the electrostatic potential. The built-in electric field of 0.10 V/Å not only significantly increases the valley splitting, but also changes its sign. Why is the regulation effect of the 0.10 V/Å built-in electric field on valley splitting much better than that of the external electric field? The important reason is the difference in SOC strength between S and Se atoms, in which the S and Se atoms are 1.8 meV and 4.0 meV, respectively.

E. Ferroelectric substrate induced transformation into the altermagnet

A third method to achieve altermagnets is by constructing heterostructures, in which the heterostructure is naturally broken PT symmetry. In order to explore the regulation of substrate on valley splitting, we choose the ferroelectric substrate Al_2S_3 and $VPSe_3$ to form the heterostructure. The lattice constant of Al_2S_3 is 3.59 Å. We find that the lattice mismatch rate of the 1×1 unit cell of $VPSe_3$ matching the $\sqrt{3} \times \sqrt{3}$ Al_2S_3 is only 0.3%. As shown in Figs. 5(a) and 5(e) and Fig. S5 [39], four typical configurations are considered: top-S, top-Al, bridge, and hollow configuration. As listed in Table SII [39], the layer spacing in all configurations is 3.24–3.82 Å, which indicates the interlayer is typically weak vdW interaction. In addition, all configurations exhibit an out-of-plane MAE, as listed in Table SIII [39]. From the relative total energy in Table SIV [39], the top-S and top-Al are the most stable P↑ and P↓ configurations, respectively.

In the following, we take top-S configuration as an example for detailed analysis. When the ferroelectric polarization of Al_2S_3 is P↑, the spin-polarized band structure is illustrated in Fig. 5(b). The VBM and CBM are located at $K-\Gamma$ path and K/K' point; simultaneously, the CBM of K and K' points exhibit valley degeneracy. When the P↑ switches P↓, as shown in Fig. 5(f), the CBM becomes the M point, while the VBM remains on the $K-\Gamma$ path. Very interestingly, the valley of VBM shows degeneracy, which is not a high symmetric point. Most importantly, as shown in Figs. 5(c) and 5(g), both P↑ and P↓ configurations produce spin splitting. This confirms the feasibility of our mechanism for realizing the altermagnet. When the SOC is included, Fig. 5(d) shows the band structure of P↑. The valley polarization direction is tuned by the Al_2S_3; however, the magnitude has barely changed. When the ferroelectric polarization of Al_2S_3 becomes P↓, as shown in Fig. 5(h), the valley splitting of 9.58 meV occurs at the VBM.

To understand the origin of VBM and CBM valley splitting, as shown in Fig. S6 [39], we calculate the orbital-resolved band structure of top-S configuration $VPSe_3/Al_2S_3$. The CBM valley splitting comes from the Se atom liked monolayer $VPSe_3$, while the VBM valley splitting is contributed by $d_{x^2-y^2} + d_{xy}$ of V atoms. We use $|\psi_v^\tau\rangle = \frac{1}{\sqrt{2}}(|d_{xy}\rangle + i\tau|d_{x2-y2}\rangle) \otimes |\uparrow\rangle$ as the orbital basis to construct

an effective Hamiltonian. The derivation is consistent. Here, we only give the conclusion:

$$E_v^S - E_v^{S'} = i\langle d_{xy}|\hat{H}^0_{\mathrm{SOC}}|d_{x2-y2}\rangle - i\langle d_{x2-y2}|\hat{H}^0_{\mathrm{SOC}}|d_{xy}\rangle \approx 4\alpha, \tag{2}$$

where $\hat{L}_z|d_{xy}\rangle = -2i\hbar|d_{x2-y2}\rangle$, $\hat{L}_z|d_{x2-y2}\rangle = 2i\hbar|d_{xy}\rangle$, and $\alpha = \lambda\langle d_{x2-y2}|\hat{S}_{z'}|d_{x2-y2}\rangle$.

It should be pointed out that the valley-dependent spin splitting occurs with the lower symmetry and SOC. Therefore, the anomalous valley Hall effect will be observed. As shown in Fig. 5(i), the spin down electron of the K valley will be generated and accumulate on one boundary in the electron doping condition for the P↑. On the contrary, in the hole doping case, the spin up hole of the S valley will also be produced and accumulate on same boundary for the P↓ [see Fig. 5(j)]. Furthermore, Fig. 5(k) shows the location of valley splits under two polarization states in the first Brillouin zone. All configurations of valley splitting are listed in Table V [39]. Note that the same phenomenon appears for other configurations, as shown in Figs. S7 and S8 [39]. This means that ferroelectric substrate Al_2S_3 can effectively tune the direction and magnitude of $VPSe_3$ valley polarization. More interestingly, the ferroelectric polarization can switch the altermagnetism effect, which indicates the ferroelectric polarization is coupled to the altermagnetic spin splitting.

III. CONCLUSION

In summary, we present a strategy for realizing the altermagnet in 2D material. We use an electric field, Janus structure, and ferroelectric substrate to make the upper and lower atoms asymmetric, while the *PT* symmetry of the AFM state is broken, resulting in a transition to the altermagnetic state. Based on the symmetry analysis and DFT calculation, the mechanism is proved to be feasible in monolayer $VPSe_3$. The magnetic ground state of monolayer $VPSe_3$ is an AFM state, which exhibits a spontaneous valley splitting of 2.91 meV. The electric field, the Janus structure, and the ferroelectric substrate can effectively break the *PT* symmetry, so that the band structure can exhibit spin splitting at the $\Gamma-KM/2-\Gamma$ path. This proves that multiple physical fields can transform monolayer $VPSe_3$ from an AFM to altermagnetic state. Moreover, the electric field can adjust the magnitude of valley splitting, while the Janus structure can regulate both the magnitude and direction of valley splitting. For the ferroelectric substrate Al_2S_3, the valley polarization direction is effectively tuned and the magnitude hardly changes under the P↑. However, when the ferroelectric polarization of Al_2S_3 switches from P↑ to P↓, the valley splitting significantly increases. In addition, the ferroelectric polarization can switch altermagnetic effect and realize anomalous valley Hall effect. Our work not only provides a route to realize the altermagnet in a 2D system, but also an efficient way to tune valley splitting.

ACKNOWLEDGMENTS

This work is supported by the National Natural Science Foundation of China (Grants No. 12474238 and No. 12004295). P.L. also acknowledges support from the China Postdoctoral Science Foundation funded project (Grant No. 2022M722547), the Fundamental Research Funds for the Central Universities (Grant No. xzy012025031), the Open Project of State Key Laboratory of Silicon and Advanced Semiconductor Materials (Grant No. SKL2024-10), and the Open Project of State Key Laboratory of Surface Physics (Grant No. KF2024_02).

DATA AVAILABILITY

The data that support the findings of this article are not publicly available. The data are available from the authors upon reasonable request.

[1] H. Y. Ma, M. Hu, N. Li, J. Liu, W. Yao, J. F. Jia, and J. Liu, Multifunctional antiferromagnetic materials with giant piezomagnetism and noncollinear spin current, Nat. Commun. **12**, 2846 (2021).

[2] L. Šmejkal, J. Sinova, and T. Jungwirth, Beyond conventional ferromagnetism and antiferromagnetism: A phase with nonrelativistic spin and crystal rotation symmetry, Phys. Rev. X **12**, 031042 (2022).

[3] L. Šmejkal, J. Sinova, and T. Jungwirth, Emerging research landscape of altermagnetism, Phys. Rev. X **12**, 040501 (2022).

[4] Y. P. Zhu, X. Chen, X. R. Liu, Y. Liu, P. Liu, H. Zha, G. Qu, C. Hong, J. Li, Z. Jiang, X. M. Ma, Y. J. Hao, M. Y. Zhu, W. Liu, M. Zeng, S. Jayaram, M. Lenger, J. Ding, S. Mo, K. Tanaka, M. Arita, Z. Liu, M. Ye, D. Shen, J. Wrachtrup, Y. Huang, R. H. He, S. Qiao, Q. Liu, and C. Liu, Observation of plaid-like spin splitting in a noncoplanar antiferromagnet, Nature (London) **626**, 523 (2024).

[5] J. Krempasky, L. Smejkal, S. W. DSouza, M. Hajlaoui, G. Springholz, K. Uhlirova, F. Alarab, P. C. Constantinou, V. Strocov, D. Usanov, W. R. Pudelko, R. G. Hernandez, A. B. Hellenes, Z. Jansa, H. Reichlova, Z. Soban, R. D. G. Betancourt, P. Wadley, J. Sinova, D. Kriegner, J. Minar, J. H. Dil, and T. Jungwirth, Altermagnetic lifting of Kramers spin degeneracy, Nature (London) **626**, 517 (2024).

[6] L. Šmejkal, A. B. Hellenes, R. Gonzalez-Hernandez, J. Sinova, and T. Jungwirth, Giant and tunneling magnetoresistance in unconventional collinear antiferromagnets with nonrelativistic spin-momentum coupling, Phys. Rev. X **12**, 011028 (2022).

[7] Z. Feng, X. Zhou, L. Smejkal, L. Wu, Z. Zhu, H. Guo, R. G. Hernandez, X. Wang, H. Yan, P. Qin, X. Zhang, H. Wu, H. Chen, Z. Meng, L. Liu, Z. Xia, J. Sinova, T. Jungwirth, and Z. Liu, An anomalous Hall effect in altermagnetic ruthenium dioxide, Nat. Electron. **5**, 735 (2022).

[8] R. González-Hernández, L. Smejkal, K. Výborný, Y. Yahagi, J. Sinova, T. Jungwirth, and J. Železný, Efficient electrical spin splitter based on nonrelativistic collinear antiferromagnetism, Phys. Rev. Lett. **126**, 127701 (2021).

[9] S. Karube, T. Tanaka, D. Sugawara, N. Kadoguchi, M. Kohda, and J. Nitta, Observation of spin-splitter torque in collinear antiferromagnetic RuO_2, Phys. Rev. Lett. **129**, 137201 (2022).

[10] H. Bai, L. Han, X. Y. Feng, Y. J. Zhou, R. X. Su, Q. Wang, L. Y. Liao, W. X. Zhu, X. Z. Chen, F. Pan, X. L. Fan, and C. Song, Observation of spin splitting torque in a collinear antiferromagnet RuO_2, Phys. Rev. Lett. **128**, 197202 (2022).

[11] S. A. A. Ghorashi, T. L. Hughes, and J. Cano, Altermagnetic routes to majorana modes in zero net magnetization, Phys. Rev. Lett. **133**, 106601 (2024).

[12] H. G. Giil and J. Linder, Superconductor-altermagnet memory functionality without stray fields, Phys. Rev. B **109**, 134511 (2024).

[13] X. Zhou, W. Feng, R. W. Zhang, L. Smejkal, J. Sinova, Y. Mokrousov, and Y. Yao, Crystal thermal transport in altermagnetic RuO_2, Phys. Rev. Lett. **132**, 056701 (2024).

[14] J. Ding, Z. Jiang, X. Chen, Z. Tao, Z. Liu, T. Li, J. Liu, J. Sun, J. Cheng, J. Liu, Y. Yang, R. Zhang, L. Deng, W. Jing, Y. Huang, Y. Shi, M. Ye, S. Qiao, Y. Wang, Y. Guo, D. Feng, and D. Shen, Large band splitting in g-wave altermagnet CrSb, Phys. Rev. Lett. **133**, 206401 (2024).

[15] Z. Q. Wang, Z. Q. Li, L. Sun, Z. Y. Zhang, K. He, H. Niu, J. Cheng, M. Yang, X. Yang, G. Chen, Z. Yuan, H. F. Ding, and B. F. Miao, Inverse spin Hall effect dominated spin-charge conversion in (101) and (110)-oriented RuO_2 films, Phys. Rev. Lett. **133**, 046701 (2024).

[16] L. Bai, W. Feng, S. Liu, L. Sejkal, Y. Mokrousov, and Y. Yao, Altermagnetism: Exploring new frontiers in magnetism and spintronics, Adv. Funct. Mater. **34**, 2409327 (2024).

[17] R.-W. Zhang, C. Cui, R. Li, J. Duan, L. Li, Z.-M. Yu, and Y. Yao, Predictable gate-field control of spin in altermagnets with spin-layer coupling, Phys. Rev. Lett. **133**, 056401 (2024).

[18] W. Sun, H. Ye, L. Liang, N. Ding, S. Dong, and S. S. Wang, Stacking-dependent ferroicity of a reversed bilayer: Altermagnetism or ferroelectricity, Phys. Rev. B **110**, 224418 (2024).

[19] X. Duan, J. Zhang, Z. Zhu, Y. Liu, Z. Zhang, I. Zutic, and T. Zhou, Antiferroelectric altermagnets: Antiferroelectricity alters magnets, Phys. Rev. Lett. **134**, 106801 (2025).

[20] Z. Zhu, X. Duan, J. Zhang, B. Hao, I. Zutic, and T. Zhou, Two-dimensional ferroelectric altermagnets: From model to material realization, arXiv:2504.06258.

[21] W. Xun, X. Liu, Y. Zhang, Y. Z. Wu, and P. Li, Stacking-, strain-engineering induced altermagnetism, multipiezo effect, and topological state in two-dimensional materials, Appl. Phys. Lett. **126**, 161903 (2025).

[22] D. Xiao, W. Yao, and Q. Niu, Valley-contrasting physics in graphene: Magnetic moment and topological transport, Phys. Rev. Lett. **99**, 236809 (2007).

[23] T. Cao, G. Wang, W. Han, H. Ye, C. Zhu, J. Shi, Q. Niu, P. Tan, E. Wang, B. Liu, and J. Feng, Valley-selective circular dichroism of monolayer molybdenum disulphide, Nat. Commun. **3**, 887 (2012).

[24] K. F. Mak, K. He, J. Shan, and T. F. Heinz, Control of valley polarization in monolayer MoS_2 by optical helicity, Nat. Nanotechnol. **7**, 494 (2012).

[25] H. Zeng, J. Dai, W. Yao, D. Xiao, and X. Cui, Valley polarization in MoS_2 monolayers by optical pumping, Nat. Nanotechnol. **7**, 490 (2012).

[26] W. Y. Tong, S. J. Gong, X. Wan, and C. G. Duan, Concepts of ferrovalley material and anomalous valley Hall effect, Nat. Commun. **7**, 13612 (2016).

[27] R. Peng, Y. Ma, X. Xu, Z. He, B. Huang, and Y. Dai, Intrinsic anomalous valley Hall effect in single-layer Nb_3I_8, Phys. Rev. B **102**, 035412 (2020).

[28] K. Wang, Y. Li, H. Mei, P. Li, and Z. X. Guo, Quantum anomalous Hall and valley quantum anomalous Hall effects in two-dimensional d^0 orbital XY monolayers, Phys. Rev. Mater. **6**, 044202 (2022).

[29] P. Li, C. Wu, C. Peng, M. Yang, and W. Xun, Multifield tunable valley splitting in two-dimensional MXene Cr_2COOH, Phys. Rev. B **108**, 195424 (2023).

[30] P. Li, X. Yang, Q.-S. Jiang, Y.-Z. Wu, and W. Xun, Built-in electric field and strain tunable valley-related multiple topological phase transitions in $VSiXN_4$(X = C, Si, Ge, Sn, Pb) monolayers, Phys. Rev. Mater. **7**, 064002 (2023).

[31] P. Li, B. Liu, S. Chen, W. X. Zhang, and Z. X. Guo, Progress on two-dimensional ferovalley materials, Chin. Phys. B **33**, 017505 (2024).

[32] Y. Wu, J. Tong, L. Deng, F. Luo, F. Tian, G. Qin, and X. Zhang, Coexisting ferroelectric and ferrovalley polarizations in bilayer stacked magnetic semiconductors, Nano Lett. **23**, 6226 (2023).

[33] W. Xun, C. Wu, H. Sun, W. Zhang, Y. Z. Wu, and P. Li, Coexisting magnetism, ferroelectric, and ferrovalley multiferroic in stacking-dependent two-dimensional materials, Nano Lett. **24**, 3541 (2024).

[34] S.-D. Guo, L. Zhang, Y. Zhang, P. Li, and G. Wang, Large spontaneous valley polarization and anomalous valley Hall effect in antiferromagnetic monolayer Fe_2CF_2, Phys. Rev. B **110**, 024416 (2024).

[35] Y. Wang, H. Sun, C. Wu, W. Zhang, S.-D. Guo, Y. She, and P. Li, Multifield tunable valley splitting and anomalous valley Hall effect in two-dimensional antiferromagnetic MnBr, Phys. Rev. B **111**, 085432 (2025).

[36] C. Wu, H. Sun, P. Dong, Y. Z. Wu, and P. Li, Coexisting triferroic and multiple types of valley polarization by structural phase transition in 2D materials, Adv. Funct. Mater. **35**, 2501506 (2025).

[37] H. Sun, Y. Ren, C. Wu, P. Dong, W. Zhang, Y. Z. Wu, and P. Li, Ferroelectric tuning of the valley polarized metal-semiconductor transition in $Mn_2P_2S_3Se_3/Sc_2CO_2$ van der Waals heterostructures and application to nonlinear Hall effect devices, Phys. Rev. Appl. **23**, 034032 (2025).

[38] X. W. Shen, W. Y. Tong, S. J. Gong, and C. G. Duan, Electrically tunable polarizer based on 2D orthorhombic ferrovalley materials, 2D Mater. **5**, 011001 (2017).

[39] See Supplemental Material at http://link.aps.org/supplemental/10.1103/shvd-vmvs for the computational methods, effective Hamiltonian model, our magnetic configurations of monolayer $VPSe_3$, the valence band of monolayer $VPSe_3$ with the SOC effect, the orbital-resolved band structure with the SOC of monolayer $VPSe_3$, the energy difference between the ferromagnetic and antiferromagnetic states of monolayer $VPSe_3$ as a function of the external electric field, the side views of the $VPSe_3/Al_2S_3$ heterostructures with diverse stacking configurations under different Al_2S_3 polarization states, the orbital-resolved band structure with the SOC of top-S configuration $VPSe_3/Al_2S_3$, the spin-polarized band structures of $VPSe_3/Al_2S_3$ heterostructures, the band structure of $VPSe_3/Al_2S_3$ heterostructures with the SOC effect, the total

energy of monolayer $VPSe_3$ and $V_2P_2S_3Se_3$ different magnetic configurations relative to the AFM-Néel state, and the layer spacing, MAE, the relative total energies of different $VPSe_3/Al_2S_3$ heterostructure configurations, and the valley splitting of different $VPSe_3/Al_2S_3$ heterostructure configurations.

[40] C. Gong, L. Li, Z. Li, H. Ji, A. Stern, Y. Xia, T. Cao, W. Bao, C. Wang, Y. Wang, Z. Q. Qiu, R. J. Cava, S. G. Louie, J. Xia, and X. Zhang, Discovery of intrinsic ferromagnetism in two-dimensional van der Waals crystals, Nature (London) **546**, 265 (2017).

[41] B. Huang, G. Clark, E. N. Moratalla, D. R. Klein, R. Cheng, K. L. Seyler, D. Zhong, E. Schmidgall, M. A. McGuire, D. H. Cobden, W. Yao, D. Xiao, P. J. Herrero, and X. Xu, Layer-dependent ferromagnetism in a van der Waals crystal down to the monolayer limit, Nature (London) **546**, 270 (2017).

[42] Q. Lu, P. Li, Z. Guo, G. Dong, B. Peng, X. Zha, T. Min, Z. Zhou, and M. Liu, Giant tunable spin Hall angle in sputtered Bi_2Se_3 controlled by an electric field, Nat. Commun. **13**, 1650 (2022).

[43] P. Li, X. S. Zhou, and Z. Guo, Intriguing magnetoelectric effect in two-dimensional ferromagnetic/perovskite oxide ferroelectric heterostructure, npj Comput. Mater. **8**, 20 (2022).

[44] L. Zhang, J. Yu, M. Yang, Q. Xie, H. Peng, and Z. Liu, Janus graphene from asymmetric two-dimensional chemistry, Nat. Commun. **4**, 1443 (2013).

[45] A. Y. Lu, H. Zhu, J. Xiao, C. P. Chuu, Y. Han, M. H. Chiu, C. C. Cheng, C. W. Yang, K. H. Wei, Y. Yang, Y. Wang, D. Sokaras, D. Nordlund, P. Yang, D. A. Muller, M. Y. Chou, X. Zhang, and L. J. Li, Janus monolayers of transition metal dichalcogenides, Nat. Nanotechnol. **12**, 744 (2017).

[46] Y.-C. Lin, C. Liu, Y. Yu, E. Zarkadoula, M. Yoon, A. A. Puretzky, L. Liang, X. Kong, Y. Gu, A. Strasser, H. M. Meyer III, M. Lorenz, M. F. Chisholm, I. N. Ivanov, C. M. Rouleau, G. Duscher, K. Xiao, and D. B. Geohegan, Low energy implantation into transition-metal dichalcogenide monolayers to form janus structures, ACS Nano **14**, 3896 (2020).

[47] H. Tang, W. Li, L. Pan, K. Tu, F. Du, T. Qiu, J. Yang, C. P. Cullen, N. McEvoy, C. Zhang, and A. Robust, Freestanding MXene-sulfur conductivepaper for long-lifetime Li-S Batteries, Adv. Funct. Mater. **29**, 1901907 (2019).